CONTROLLING INFLUENCE OF MAGNETIC FIELD ON SOLAR WIND OUTFLOW: AN INVESTIGATION USING CURRENT SHEET SOURCE SURFACE MODEL

B. PODUVAL
Space Science Institute, Boulder, CO 80303, USA; bpoduval@spacescience.org

ABSTRACT

This Letter presents the results of an investigation into the controlling influence of large-scale magnetic field of the Sun in determining the solar wind outflow using two magnetostatic coronal models: current sheet source surface (CSSS) and potential field source surface. For this, we made use of the Wang and Sheeley inverse correlation between magnetic flux expansion rate (FTE) and observed solar wind speed (SWS) at 1 au. During the period of study, extended over solar cycle 23 and beginning of solar cycle 24, we found that the coefficients of the fitted quadratic equation representing the FTE–SWS inverse relation exhibited significant temporal variation, implying the changing pattern of the influence of FTE on SWS over time. A particularly noteworthy feature is an anomaly in the behavior of the fitted coefficients during the extended minimum, 2008–2010 (CRs 2073–2092), which is considered due to the particularly complex nature of the solar magnetic field during this period. However, this variation was significant only for the CSSS model, though not a systematic dependence on the phase of the solar cycle. Further, we noticed that the CSSS model demonstrated better solar wind prediction during the period of study, which we attribute to the treatment of volume and sheet currents throughout the corona and the more accurate tracing of footpoint locations resulting from the geometry of the model.

Key words: solar wind – Sun: corona – Sun: magnetic fields

1. INTRODUCTION

In the theory of solar wind put forth by Parker (1958) there exists a reference height in the corona beyond which plasma takes control over the magnetic field. Location of this reference height, better known as "source surface," is crucial to quantitatively model the background solar wind conditions in the corona and the heliosphere. In magnetostatic models the source surface is placed as low as 2.5 $R_\odot$ (potential field source surface, PFSS) and as high as 15 $R_\odot$ (current sheet source surface, CSSS). It is well established that coronal holes, where magnetic field lines are open into the heliosphere, are the sources of fast solar wind (e.g., Zirker 1977a, 1977b), but the origin of slow solar wind is still being debated, though regions surrounding closed magnetic field configuration are considered to be the major sources (e.g., Ohmi 2003; Cranmer et al. 2013).

Studies in the 1970s using *Skylab* data suggested that regions with low areal expansion corresponded well with high-speed streams observed at Earth (Kopp & Holzer 1976; Levine et al. 1977). Nearly two decades later, Wang and Sheeley (WS) established an empirical inverse relationship between the in-ecliptic solar wind speed (SWS) and the expansion rates of magnetic flux tubes (FTEs) defined as

$$\mathrm{FTE} = \left(\frac{R_\odot}{R_{\mathrm{ss}}}\right)^2 \frac{B(\mathrm{phot})}{B(\mathrm{ss})} \qquad (1)$$

where $B(\mathrm{phot})$ and $B(\mathrm{ss})$ are the photospheric and the source surface magnetic fields at radii $R_\odot$ and R_{ss}. Since FTE is proportional to the ratio of the photospheric and the source surface magnetic fields, this suggests that centers of coronal holes corresponding to low values of FTEs give rise to fast wind while the boundaries, with large FTEs, are the sources of slow solar wind (e.g., Wang & Sheeley 1990). This inverse relation between FTE and SWS is for certain ranges of these quantities as shown in Wang et al. (1997, Table 1).

Zhao & Hoeksema (1995) have demonstrated that the heliospheric magnetic field (HMF) polarity and strength predicted using the CSSS model they developed matched better with observed values near the Earth than other models they used in the study. The model has further been validated for solar wind prediction by Poduval & Zhao (2014, hereafter Paper I). We have shown in Paper I that the CSSS predictions based on the WS FTE–SWS relationship (Table 1 in Wang et al. 1997) are more accurate than the PFSS predictions, by a factor close to 2. Encouraged by this finding, we employed the CSSS model to investigate the influence of global magnetic field in determining the solar wind outflow and compared the results with those obtained using PFSS model.

In Section 2, we present the models and the data used. The methodology and the results are described in Section 3. Results are discussed in Section 4, followed by our concluding remarks in Section 5.

2. MODELS AND DATA

In order to compute FTEs we need to know the magnetic field in the lower corona. Measuring coronal magnetic field is extremely difficult and routine measurements remained nearly impossible due to the extremely low intensity of coronal magnetic field and certain technical difficulties until the Coronal Multi-Channel Polarimeter (CoMP; Tomczyk et al. 2008; Bak-Steslicka et al. 2013; Judge et al. 2013; Kramar et al. 2016). Though CoMP is capable of measuring coronal magnetic field as a line of sight integration, producing routine synoptic maps of coronal magnetic fields, similar to the photospheric maps, is still a challenge. Further, the in situ solar wind measurements closest to the Sun made by a spacecraft so far is 0.3 au (~65$R_\odot$), by Helios 1 and Helios 2 in the 1970s and the 1980s (Schwenn & Marsch 1990). Therefore, we need to compute the coronal magnetic fields from the photospheric field using models.

The main difference between the two magnetostatic models is that the electric currents in the region bounded by the photosphere and the source surface are considered to be negligible in the PFSS model (Hoeksema 1984 and the references therein), whereas both sheet and volume currents are effectively incorporated into the CSSS model (Zhao & Hoeksema 1995 and the references therein). Both the models employ spherical harmonic expansion to obtain coronal magnetic field at various heights in the atmosphere. The only input to both the models is the synoptic map of photospheric magnetic field. We placed the cusp surface at a heliocentric distance of 2.5 $R_\odot$ and the source surface at 15 $R_\odot$ in the CSSS model, while the source surface in the PFSS was placed at 2.5 $R_\odot$—as in Paper I. For detailed descriptions of CSSS model refer to Zhao & Hoeksema (1993, 1994, 1995) and for an account of its advantages, see Paper I.

We computed the FTEs and predicted the SWS for solar cycles 23 and early 24 (two years), i.e., from 1996 to 2010 (CRs: 1912–2104), using the *SOHO*/MDI synoptic maps (Scherrer et al. 1995) as input to the models. These synoptic maps have their polar fields filled by interpolation (Sun et al. 2011). The original MDI data, 3600×1800, have been scaled down to 360×180, leaving a spatial resolution of 1° in latitude and Carrington longitude, to reduce computational overhead. No MDI data are available for CRs 1938–1941 and the polar field corrected data for CRs 1942 and 1945 are also missing. Since the inverse mapping of observed solar wind can land on a previous rotation, we excluded CRs 1938–1946 (1998 July 5–1999 March 7) from the present study. MDI data are available for download from http://soi.stanford.edu/magnetic/index6.html.

For a comparative study we used synoptic maps from Wilcox Solar Observatory (WSO), Mount Wilson Observatory (MWO), and Synoptic Optical Long-term Investigations of the Sun (SOLIS): National Solar Observatories (NSO). We also used NSO/Kitt Peak data (KPK) for the period CRs 1912–2006, before SOLIS data became available. No Helioseismic and Magnetic Imager (HMI) data are available during the period of study.

In order to obtain the functional relationship between FTE and SWS, we need solar wind data at 1 au. For this, we made use of the daily averaged OMNI data that are a compilation from a number of spacecraft in the ecliptic plane, for the same period. The OMNI data are available at http://omniweb.gsfc.nasa.gov/.

3. METHOD AND RESULTS

The method we adopted in this Letter is similar to that in Paper I and we present a brief summary of the steps involved. As our aim is to infer the temporal variation of the dependence of SWS on FTE, we need to establish the connection between the two. For this, we mapped the observed solar wind back to the Sun to determine their coronal sources and the corresponding photospheric footpoints, and computed FTEs corresponding to observed SWS. This was done in two steps as described in Paper I: ballistic inverse mapping and, then, tracing back to the photosphere along the magnetic field lines using the models.

The heliocentric distance of the source surface in the CSSS model is far out in the atmosphere (15 $R_\odot$) where the solar wind is close to attaining its supersonic speed and becoming radial (Parker 1958; Zhao & Hoeksema 2010), but the expansion rate

of the magnetic field that determines SWS is significant and relevant only in the lower corona (as pointed out in Paper I). Since magnetic field become open around 2.5 $R_\odot$, which corresponds to the cusp points of helmet streamers (e.g., Zhao & Hoeksema 1995), this is a convenient and meaningful distance for computing FTE for both the models and making a comparison. As in Paper I, we used the same function for both the models.

We split the period of study into different phases as follows. Phase $P1$: CRs 1912–1936; data gap: CRs1937–1946, no MDI data are available; Phase $P2$: CRs 1947–1985 (the ascending-maximum-descending phase of solar cycle 23); Phase $P2a$: CRs 1986–2072; Phase $P3$: CRs 2073–2092 (*extended minimum*) and Phase $P3a$: CRs 2093–2104. Phase $P1$ was further divided into 7 subperiods of 4 rotations, with the exception of the first one that includes 5 rotations. Phases $P2$ and $P2a$ were split into 41 subperiods of 3 rotations each, except the last two which include 4 and 5 rotations, respectively. Phases $P3$ and $P3a$ were divided into 8 subperiods, each containing 4 rotations. We then assigned SWS to ranges of FTEs according to the WS inverse relation and obtained the best-fit quadratic functions describing the $\log_{10}(|FTE|)$–SWS relationship for each of the 3- or 4-rotation subgroups in all the 5 phases. Explicitly, this function is

$$\mathrm{SWS_{pred}} = a \times f^2 + b \times f + c \tag{2}$$

where the coefficients a, b, and c, represent the quadratic, the linear, and the constant terms, $f = \log_{10}(|FTE|)$ is the FTE, and $\mathrm{SWS_{pred}}$ is the predicted speed. Using (2), we obtained $\mathrm{SWS_{pred}}$ for individual Carrington rotations for the entire period of study. Also, we computed the root mean square errors (RMSEs) between $\mathrm{SWS_{pred}}$ and observed SWS; their ratios, *rmseratio*; and correlation coefficients between SWS and $\mathrm{SWS_{pred}}$ to evaluate the predictive capabilities of two models as described in Paper I.

As pointed out in Paper I, the correlation coefficient between observed and predicted SWS alone is inadequate to evaluate the predictive capabilities of the models or the accuracy of their predictions. Correlation between two quantities, in general, implies how the variations in one affects the other. Arguably, in the present context of forecasting using models, what matters is the accuracy. Even though the variations in the two quantities follow the same (or inverse) pattern, the predicted and observed values may not be close to each other to be within the uncertainty level of statistical significance. We found the *rms* errors between observations and predictions a better metric for evaluating the performances of the models.

Figures 1 and 2 depict the coefficients of the fitted quadratic functions during the entire period of study: 1996–2010 (CRs 1912–2104). Here, regions marked as $P1$, $P2$, and $P3$ are three distinct phases we discuss below, and the X-axis ticks correspond to the starting rotation in each of the subperiods described above. Results using MDI data are shown in the top panel of Figure 1, where the space between $P1$ and $P2$ represent the data gap (CRs 1937–1945), The bottom panel of Figure 1 depicts combined KPK (rotations on the left-hand side of the solid vertical line) and SOLIS (for the remaining rotations, starting from CR2007) data. In Figure 2, MWO (top panel) and WSO (bottom panel) results are presented. Figures 3(a) and (b) depict Phases $P2$ and $P3$, presenting the *rmseratios* (top), the *rms* errors (middle), and the correlation coefficients between SWS and $\mathrm{SWS_{pred}}$ (bottom). The solid
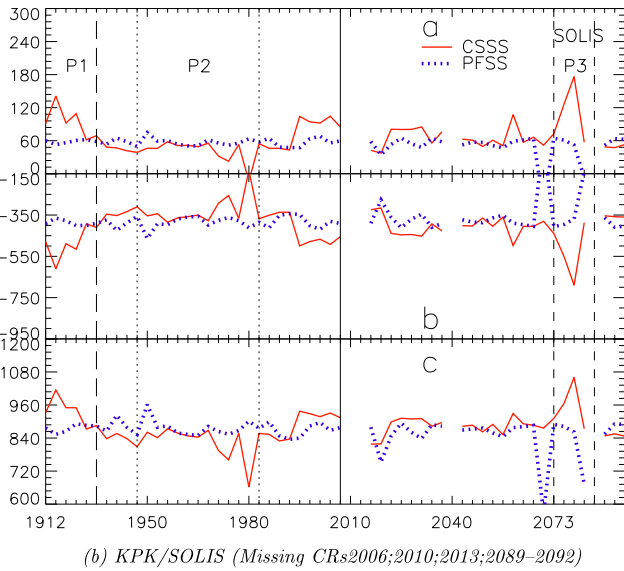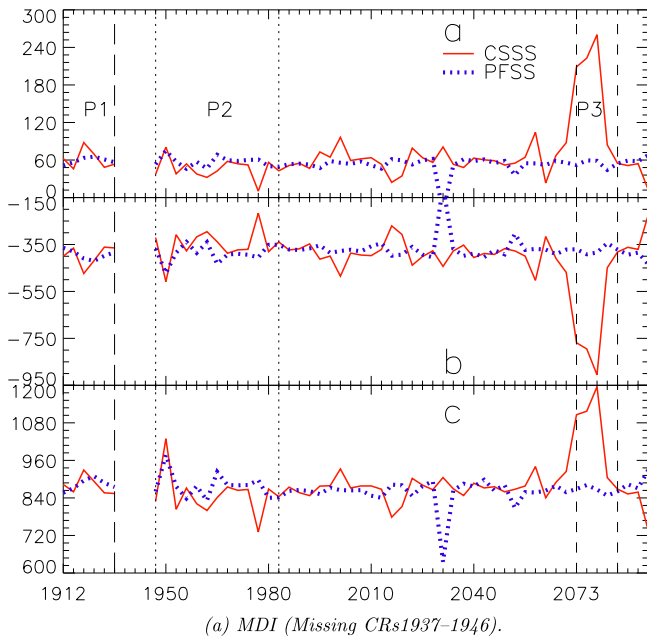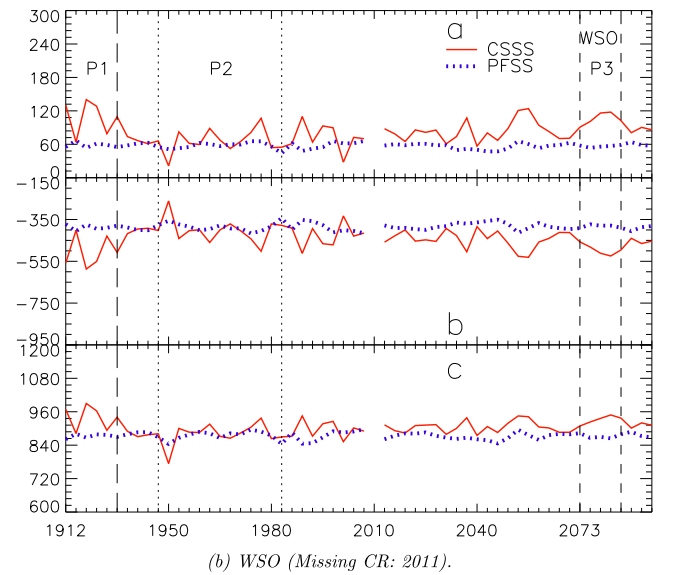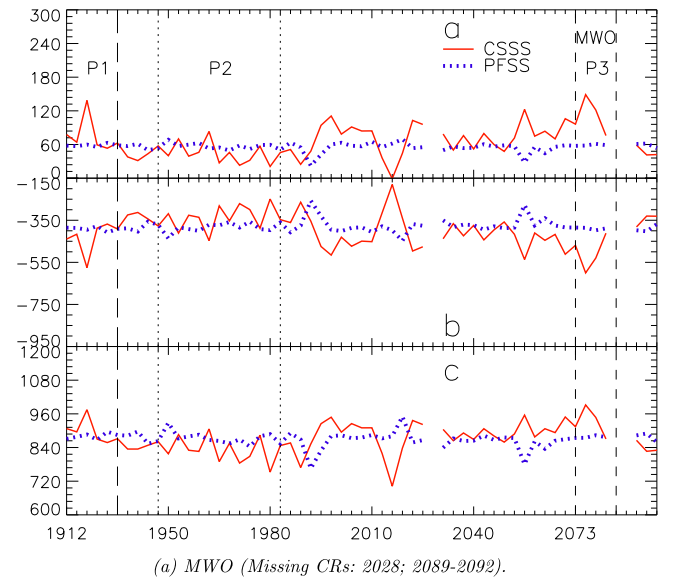
Figure 1. Temporal variations of coefficients *a*, *b*, and *c* of the best-fit quadratic functions obtained for CSSS (solid line) and PFSS (dotted line) models during the period of study, 2008–2010 (CRs 1912–2104). Results for MDI data are shown in top panel. We used KPK synoptic maps for rotations on the left of the sold vertical line (bottom panel) and SOLIS data for the remaining rotations (after CR 2006).

Figure 2. Same as Figure 1, but for MWO (top) and WSO (bottom) synoptic maps.

horizontal line in the top panel corresponds to *rmseratio* = 1, which implies that both the models are comparable. Values above this line indicate CSSS predictions are better than PFSS.

Figure 4 shows the fitted quadratic functions for Phases *P*2 (panel (a)) and *P*3 (panel (b)). Here, $\log_{10}(|\mathrm{FTE}|)$ is on the *X*-axis and SWS on the *Y*-axes. The fitted curve, the SWSs assigned according to WS empirical relation, and the predicted SWS are represented by the solid lines, the diamonds, and the crosses, respectively.

In all the figures, solid lines depict the CSSS model, while dotted lines represent the PFSS model. Figure 5 presents neutral lines (HCS) at 2.5 $R_\odot$ in the CSSS model, computed with MDI (solid lines), WSO (dashed lines), and SOLIS (dotted–dashed line) synoptic maps. The dotted lines depict the

same obtained with the PFSS model and WSO synoptic maps (courtesy of J. T. Hoeksema; http://wso.stanford.edu/synsourcel.html).

4. DISCUSSION OF THE RESULTS

Figures 1 and 2 depict temporal variations of the coefficients *a*, *b*, and *c* of the quadratic, the linear, and the constant terms of the fitted quadratic functions. Phase *P*1 covering CRs 1912–1936 (1996–1998) is the same period studied in Paper I using WSO and KPK synoptic maps, and the results obtained here are comparable to those. Since Phases *P*2a and *P*3a (not marked) do not exhibit any specific features to be discussed in this Letter, we focus on Phases *P*2 and *P*3.

The most noteworthy feature of Figures 1 and 2 is the dramatic difference in the behaviors of the fitted coefficients during the extended minimum (Phase *P*3). Comparing with Phase *P*2, it is evident that the temporal variations during Phase *P*3 are much larger. Further, the fluctuations are much
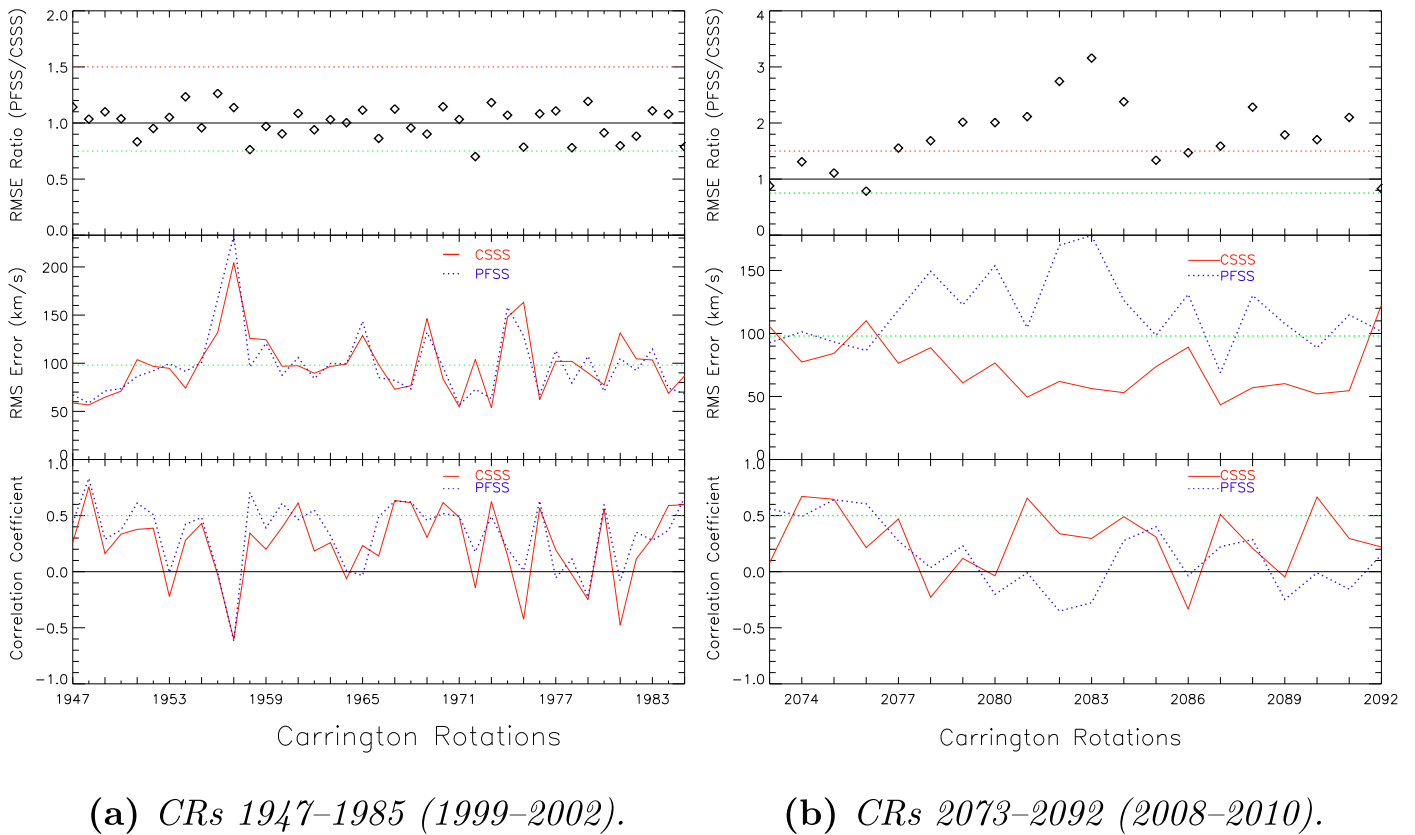
Figure 3. Comparison of solar wind predictions using CSSS (solid lines) and PFSS (dotted lines) models. Panel (a) depicts Phase *P*2 and panel (b) represents Phase *P*3. The root mean square error (RMSE) is obtained between the near-Earth observations of solar wind speed and the models predictions. Top panel: the *rmseratio* between CSSS and PFSS model. Middle panel: the *rms* errors. Bottom panel: the correlation coefficients between the observed SWS and those predicted by CSSS and PFSS models.

more significant for the CSSS model in general (except for CRs 1931–1934 in Figure 1(a); a discussion on this aspect is beyond the scope of this Letter), and in particular during Phase *P*3, where the PFSS model shows practically no variation. Comparing with the fitted coefficients for SOLIS (Figure 1(b)); and MWO and WSO (Figures 2(a) and (b)) data, we note that the temporal variation for the CSSS model is significant, though less dramatic than the MDI data. While MWO and WSO show comparable variations, the SOLIS data exhibit slightly larger fluctuations. It is not clear why the MDI variations are so pronounced (higher resolution of MDI data?), but we are further investigating this aspect.

The metrics of accuracy presented in Figure 3 greatly support this anomalous behavior of the coefficients. That is, during Phase *P*3, the CSSS predictions, on average, are nearly twice (1.7) better than PFSS predictions (top panel), with a mean *rms* error 38% less than that in the PFSS model (73 km s^{-1} for CSSS and 117 km s^{-1} for PFSS) and a mean correlation coefficient twice that of the PFSS model (0.28 for CSSS; 0.14 for PFSS).

This is further elucidated in Figure 4, where the fitted curves change from a near parabolic (when there is a strong quadratic term—larger values of *a*) to almost a straight line (when the quadratic term nearly vanishes—as *a* approaches zero), indicating the variation of the dependence of SWS on FTE.

As is clear from Figure 5, CSSS neutral lines computed using different synoptic maps are all consistent with each other in most cases. While CSSS neutral lines are much flatter, the

PFSS/WSO neutral lines have larger latitudinal extensions, evidently a consequence of the differences in the two models.

The above analysis leads us to conclude that the temporal variations in the fitted coefficients exhibited by the CSSS model during the extended minimum is a real effect caused by the changing magnetic field configurations.

We explored the physical implications of this anomalous behavior of the coefficients during Phase *P*3. It is well known that the measured polar field strength influences the modulation of the neutral line and thereby the predicted SWS. Wang et al. (2009) have shown that stronger polar fields indicate larger polar coronal holes, disappearance/shrinking of low-latitude coronal holes, and flatter HCS. Gibson et al. (2009) reported that during 2008 there existed numerous low-latitude coronal holes giving rise to frequent high-speed solar wind in the ecliptic. Further, Wang et al. (2009) showed that an increase in the polar coronal hole indicates smaller expansion factors (FTEs) and thereby an increase in the polar SWS.

The average unsigned polar field strength in the MDI, MWO, SOLIS, and WSO synoptic maps are 3.6, 5.1, 4.1, and 3.8 G, respectively, during Phase *P*3. These are about 33%–45% less than corresponding values around the minimum of solar cycle 23 (CRs 1911–1931: SOLIS data not available). Moreover, $\log_{10}(|FTE|)$ seems to be confined within 0.8 and 2.3 during Phase *P*3, in contrast to Phase *P*2 where the corresponding values are 0.1 and 4.0. The lower value during Phase *P*3 implies (as inferred from Table 1 of Wang et al. 1997; note that FTE is not on the logarithmic scale) SWS above 650 km s^{-1} may not have been predicted accurately; the high
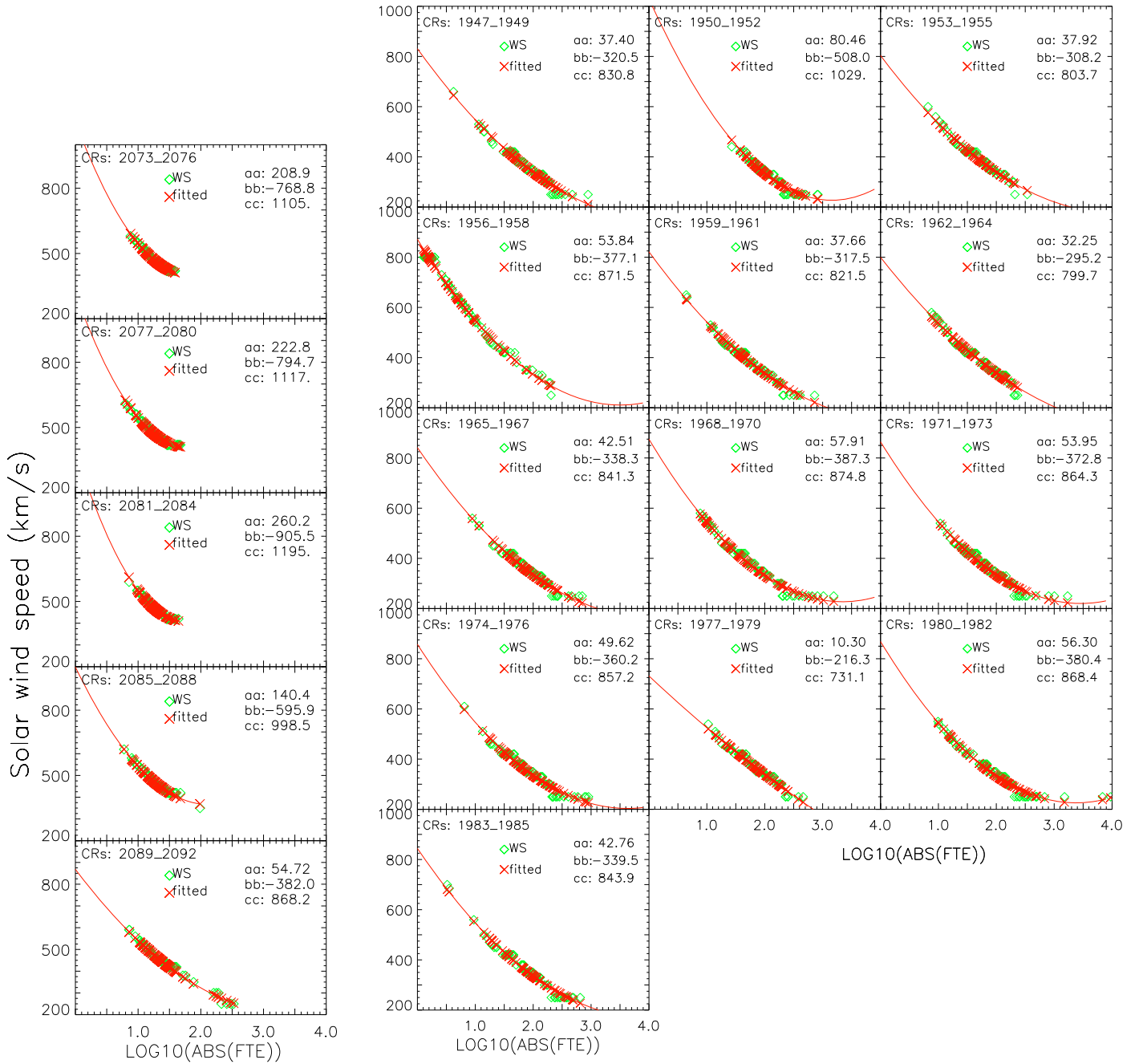
Figure 4. Best-fit quadratic function to $\log_{10}(|FTE|)$–SWS for the CSSS model. The WS predictions are represented by crosses, while the diamonds and the solid lines depict the fitted curve. The coefficients a, b, and c of the fitted quadratic functions are given at the top right-hand corner in each panel. Panel (a) represents Phase $P3$, while panel (b) depicts Phase $P2$.

values ($>950 \mathrm{\ km \ s^{-1}}$) of the y-intercept ($c$) support this, which seldom occurred in Phase $P2$ (except during 1950–1952 where it is $1029 \mathrm{\ km \ s^{-1}}$). Since polar field strengths during 2008–2010 are significantly lower than those of the past minima, the above argument of Wang et al. (2009) explains the missing lower values and thereby the temporal variations of the coefficients. Though values between 1.3 and 2.0 (as in $P3$) are sufficient to predict most of the observed slow wind, the narrow range of $\log_{10}(FTE)$ during Phase $P3$ questions the source of solar wind during this period: small, low-latitude coronal holes and/or pseudostreamers, rather than polar coronal holes, which is the typical solar minimum source of solar wind. A more

detailed analysis of these aspects is beyond the scope of this Letter but is the subject of an accompanying paper.

5. CONCLUDING REMARKS

The electric currents in the lower corona manifest themselves as the many structures seen in coronal images (Hundhausen 1972; Zhao et al. 2002). At some height in the coronal atmosphere, around 2.5 $R_\odot$, the source surface location in PFSS and the cusp surface in CSSS models, closed field configurations are no longer found and all the field lines are open, with a current sheet at the polarity inversion region. Beyond this height, the solar wind controls the magnetic field,
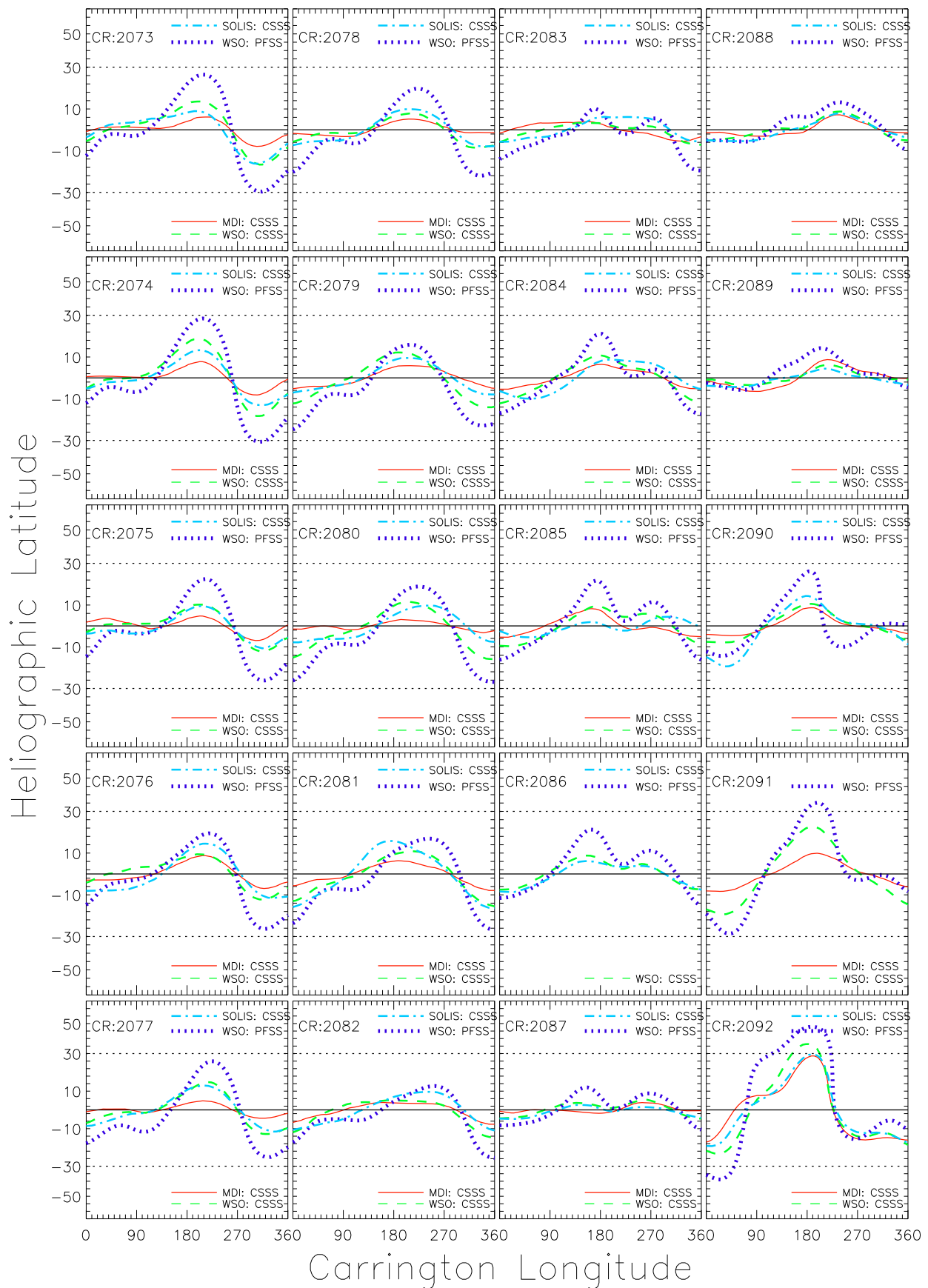
Figure 5. Comparison of neutral lines computed using the CSSS model and MDI (solid line), WSO (dashed lines), and SOLIS (dotted–dashed lines), and the PFSS model with WSO (dotted lines) synoptic maps. MDI data for CR 2086 and SOLIS data for CRs 2090 and 2091 have data gaps and, therefore, are excluded from the study.

carrying it into the heliosphere to form HMF (Parker 1958; Hundhausen 1972). This interplay between the magnetic field and the solar wind at the base of the corona is likely to be reflected in the spatial and temporal variations of FTE, which obviously is controlled by magnetic fields. The spatial variations of FTEs are incorporated into the well-known WS empirical relationship. The present Letter investigates the temporal variations of the FTE–SWS relationship during solar cycle 23 and beginning of cycle 24 and attempts to infer the controlling influence of the coronal magnetic field in determining the solar wind outflow. We note that:

1. There exists a subtle, significant temporal variation of the FTE–SWS dependence that is clearly reflected in the behavior of the best-fit quadratic equation for these variables, when CSSS model is employed to compute FTEs. This variation is particularly pronounced when MDI synoptic maps are used.
2. Similar, but less dramatic, variations exhibited by other synoptic maps indicate that this is a real effect, possibly caused by the changing characteristics of the solar magnetic field (e.g., Gibson et al. 2009; Wang et al. 2009) during this period.
3. Such a variation is nearly negligible for the PFSS model.
4. The CSSS model is sensitive to subtle characteristics of the solar magnetic field that, in turn, is reflected in its better predictive capability (Figure 3) during all phases of a solar cycle.

Though the extent of fluctuations in the coefficients, particularly during the extended minimum, is different for different synoptic maps, it is to be emphasized that PFSS model did not show any significant fluctuations throughout the period of study, even during the extended minimum.

We argue that the treatment of electric currents in the CSSS model provides a more realistic coronal scenario than the potential field approximation in the PFSS model. Combined with the more accurate tracing of solar wind sources owing to its geometry (as we pointed out in Paper I), we conclude that the CSSS model is an effective and robust tool for investigating the controlling influence of the global solar magnetic field on the solar wind outflow. A more detailed investigation, including optimization of the free parameters of the CSSS model, is currently underway.

REFERENCES

Bak-Steslicka, U., Gibson, S. E., Fan, Y., et al. 2013, ApJL, 770, L28
Cranmer, S. R., van Ballegooijen, A. A., & Woolsey, L. N. 2013, ApJ, 767, 125
Gibson, S. E., Kozyra, J. U., de Toma, G., et al. 2009, JGR, 114, A09105
Hoeksema, J. T. 1984, PhD thesis, Stanford Univ.
Hundhausen, A. J. 1972, Coronal Expansion and Solar Wind, Vol. 5 (New York: Springer)
Judge, P. G., Habbal, S., & Landi, E. J. 2013, SoPh, 288, 467
Kopp, R. A., & Holzer, T. E. 1976, SoPh, 49, 43
Kramar, M., Lin, H., & Tomczyk, S. 2016, ApJL, 819, L36
Levine, R. H., Altschuler, M. D., & Harvey, J. W. 1977, JGR, 82, 1061
Ohmi, T. 2003, PhD thesis, Nagoya Univ.
Parker, E. N. 1958, ApJ, 128, 664
Poduval, B., & Zhao, X.-P. 2014, ApJL, 782, L22
Scherrer, P. H., Bogart, R. S., Bush, R. I., et al. 1995, SoPh, 162, 129
Schwenn, R., & Marsch, E. 1990, Physics and Chemistry in Space, Vol. 20, Physics of the Inner Heliosphere I: Large Scale Phenomena, ed. R. Schwenn & E. Marsch (Berlin: Springer)
Sun, X., Liu, Y., Hoeksema, J. T., Hayashi, K., & Zhao, X. 2011, SoPh, 270, 9
Tomczyk, S., Card, G. L., Darnell, T., et al. 2008, SoPh, 247, 411
Wang, Y.-M., Robbrecht, E., & Sheeley, N. R., Jr. 2009, ApJ, 707, 1372
Wang, Y.-M., & Sheeley, N. R. J. 1990, ApJ, 355, 726
Wang, Y.-M., Sheeley, N. R., Jr., Phillips, J. L., & Goldstein, B. E. 1997, ApJL, 488, L51
Zhao, X. P., & Hoeksema, J. T. 1993, SoPh, 143, 41
Zhao, X. P., & Hoeksema, J. T. 1994, SoPh, 151, 91
Zhao, X. P., & Hoeksema, J. T. 1995, JGR, 100, 19
Zhao, X. P., & Hoeksema, J. T. 2010, SoPh, 266, 379
Zhao, X. P., Hoeksema, J. T., & Rich, N. B. 2002, AdSpR, 29, 411
Zirker, J. B. 1977a, in Coronal Holes and High-speed Wind Streams, ed. J. B. Zirker (Boulder, CO: Colorado Assoc. Univ. Press), 1
Zirker, J. B. 1977b, RvGSP, 16, 257